

# Multimodal photoacoustic and optical coherence tomography scanner using an all optical detection scheme for 3D morphological skin imaging

Edward Z. Zhang,<sup>1</sup> Boris Povazay,<sup>2</sup> Jan Laufer,<sup>1</sup> Aneesh Alex,<sup>2</sup> Bernd Hofer,<sup>2</sup> Barbara Pedley,<sup>3</sup> Carl Glittenberg,<sup>4</sup> Bradley Treeby,<sup>1</sup> Ben Cox,<sup>1</sup> Paul Beard,<sup>1</sup> and Wolfgang Drexler<sup>2,\*</sup>

<sup>1</sup>Department of Medical Physics and Bioengineering, University College London, Gower Street, London, WC1E 6BT, UK

<sup>2</sup>Center for Medical Physics and Biomedical Engineering, 4L, Medical University Vienna, Waehringer Guertel 18-20, A-1090 Vienna, Austria

<sup>3</sup>UCL Cancer Institute, Paul O'Gorman Building, University College London, 72 Huntley St, London WC1E 6BT, UK

<sup>4</sup>Rudolf Foundation Clinic Vienna, Department of Ophthalmology, Ludwig Boltzmann Institute, Vienna, Austria  
\*[wolfgang.drexler@medunivien.ac.at](mailto:wolfgang.drexler@medunivien.ac.at)

**Abstract:** A noninvasive, multimodal photoacoustic and optical coherence tomography (PAT/OCT) scanner for three-dimensional *in vivo* (3D) skin imaging is described. The system employs an integrated, all optical detection scheme for both modalities in backward mode utilizing a shared 2D optical scanner with a field-of-view of  $\sim 13 \times 13$  mm<sup>2</sup>. The photoacoustic waves were detected using a Fabry Perot polymer film ultrasound sensor placed on the surface of the skin. The sensor is transparent in the spectral range 590-1200 nm. This permits the photoacoustic excitation beam (670-680 nm) and the OCT probe beam (1050 nm) to be transmitted through the sensor head and into the underlying tissue thus providing a backward mode imaging configuration. The respective OCT and PAT axial resolutions were 8 and 20  $\mu$ m and the lateral resolutions were 18 and 50-100  $\mu$ m. The system provides greater penetration depth than previous combined PA/OCT devices due to the longer wavelength of the OCT beam (1050 nm rather than 829-870 nm) and by operating in the tomographic rather than the optical resolution mode of photoacoustic imaging. Three-dimensional *in vivo* images of the vasculature and the surrounding tissue micro-morphology in murine and human skin were acquired. These studies demonstrated the complementary contrast and tissue information provided by each modality for high-resolution 3D imaging of vascular structures to depths of up to 5 mm. Potential applications include characterizing skin conditions such as tumors, vascular lesions, soft tissue damage such as burns and wounds, inflammatory conditions such as dermatitis and other superficial tissue abnormalities.

© Copyright 2011 Optical Society of America

**OCIS codes:** (110.0110) Imaging systems; (130.0130) Integrated optics; (140.0140) Lasers and laser optics; (170.0170) Medical optics and biotechnology; (290.0290) Scattering; (320.0320) Ultrafast optics

---

## References and links

1. P. C. Beard, "Biomedical photoacoustic imaging," *Interface Focus* **1**, 602–631 (2011).
2. J. G. Laufer, D. T. Delpy, C. E. Elwell, and P. C. Beard, "Quantitative spatially resolved measurement of tissue chromophore concentrations using photoacoustic spectroscopy: application to the measurement of blood oxygenation and haemoglobin concentration," *Phys. Med. Biol.* **52**(1), 141–168 (2007).
3. J. G. Laufer, B. Cox, E. Z. Zhang, and P. C. Beard, "Quantitative determination of chromophore concentrations from 2D photoacoustic images using a nonlinear model-based inversion scheme," *Appl. Opt.* **49**(8), 1219–1233 (2010).

4. P. C. Beard, Flow velocity measurements, UK Patent Application, PCT/GB02/04977 (2001)
5. J. Brunker and P. C. Beard, "Pulsed photoacoustic Doppler flow measurements in blood-mimicking phantoms," *Proc. SPIE* **7899**, 78991K, 78991K-10 (2011).
6. H. Fang, K. Maslov, and L. V. Wang, "Photoacoustic Doppler effect from flowing small light-absorbing particles," *Phys. Rev. Lett.* **99**(18), 184501 (2007).
7. R. A. Kruger, R. B. Lam, D. R. Reinecke, S. P. Del Rio, and R. P. Doyle, "Photoacoustic angiography of the breast," *Med. Phys.* **37**(11), 6096–6100 (2010).
8. X. Wang, Y. Pang, G. Ku, X. Xie, G. Stoica, and L. V. Wang, "Noninvasive laser-induced photoacoustic tomography for structural and functional *in vivo* imaging of the brain," *Nat. Biotechnol.* **21**(7), 803–806 (2003).
9. J. G. Laufer, E. Z. Zhang, G. Raivich, and P. C. Beard, "Three-dimensional noninvasive imaging of the vasculature in the mouse brain using a high resolution photoacoustic scanner," *Appl. Opt.* **48**(10), D299–D306 (2009).
10. C. Li, A. Aguirre, J. Gamelin, A. Maurudis, Q. Zhu, and L. V. Wang, "Real-time photoacoustic tomography of cortical hemodynamics in small animals," *J. Biomed. Opt.* **15**(1), 010509 (2010).
11. H. P. Brecht, R. Su, M. Fronheiser, S. A. Ermilov, A. Conjusteau, and A. A. Oraevsky, "Whole-body three-dimensional photoacoustic tomography system for small animals," *J. Biomed. Opt.* **14**(6), 064007 (2009).
12. E. Z. Zhang, J. G. Laufer, R. B. Pedley, and P. C. Beard, "*In vivo* high-resolution 3D photoacoustic imaging of superficial vascular anatomy," *Phys. Med. Biol.* **54**(4), 1035–1046 (2009).
13. K. Maslov, H. F. Zhang, S. Hu, and L. V. Wang, "Optical-resolution photoacoustic microscopy for *in vivo* imaging of single capillaries," *Opt. Lett.* **33**(9), 929–931 (2008).
14. C. Zhang, K. Maslov, and L. V. Wang, "Subwavelength-resolution label-free photoacoustic microscopy of optical absorption *in vivo*," *Opt. Lett.* **35**(19), 3195–3197 (2010).
15. D. Huang, E. A. Swanson, C. P. Lin, J. S. Schuman, W. G. Stinson, W. Chang, M. R. Hee, T. Flotte, K. Gregory, C. A. Puliafito, and J. G. Fujimoto, "Optical coherence tomography," *Science* **254**(5035), 1178–1181 (1991).
16. A. F. Fercher, C. K. Hitzenberger, W. Drexler, G. Kamp, and H. Sattmann, "*In vivo* optical coherence tomography," *Am. J. Ophthalmol.* **116**(1), 113–114 (1993).
17. C. K. Fercher, C. K. Hitzenberger, G. Kamp, and S. Y. El-Zaiat, "Measurement of intraocular distances by backscattering spectral interferometry," *Opt. Commun.* **117**, 43–48 (1995).
18. G. Häusler, J. M. Herrmann, R. Kummer, and M. W. Lindner, "Observation of light propagation in volume scatterers with  $10^{11}$ -fold slow motion," *Opt. Lett.* **21**(14), 1087–1089 (1996).
19. S. R. Chinn, E. A. Swanson, and J. G. Fujimoto, "Optical coherence tomography using a frequency-tunable optical source," *Opt. Lett.* **22**(5), 340–342 (1997).
20. R. K. Wang, L. An, P. Francis, and D. J. Wilson, "Depth-resolved imaging of capillary networks in retina and choroid using ultrahigh sensitive optical microangiography," *Opt. Lett.* **35**(9), 1467–1469 (2010).
21. B. J. Vakoc, R. M. Lanning, J. A. Tyrrell, T. P. Padera, L. A. Bartlett, T. Stylianopoulos, L. L. Munn, G. J. Tearney, D. Fukumura, R. K. Jain, and B. E. Bouma, "Three-dimensional microscopy of the tumor microenvironment *in vivo* using optical frequency domain imaging," *Nat. Med.* **15**(10), 1219–1223 (2009).
22. B. Herrmann, B. Hofer, C. Meier, and W. Drexler, "Spectroscopic measurements with dispersion encoded full range frequency domain optical coherence tomography in single- and multilayered non-scattering phantoms," *Opt. Express* **17**(26), 24162–24174 (2009).
23. L. Li, K. Maslov, G. Ku, and L. V. Wang, "Three-dimensional combined photoacoustic and optical coherence microscopy for *in vivo* microcirculation studies," *Opt. Express* **17**(19), 16450–16455 (2009).
24. S. Jiao, Z. Xie, H. F. Zhang, and C. A. Puliafito, "Simultaneous multimodal imaging with integrated photoacoustic microscopy and optical coherence tomography," *Opt. Lett.* **34**(19), 2961–2963 (2009).
25. S. Jiao, M. Jiang, J. Hu, A. Fawzi, Q. Zhou, K. K. Shung, C. A. Puliafito, and H. F. Zhang, "Photoacoustic ophthalmoscopy for *in vivo* retinal imaging," *Opt. Express* **18**(4), 3967–3972 (2010).
26. E. Z. Zhang, J. G. Laufer, and P. C. Beard, "Backward-mode multiwavelength photoacoustic scanner using a planar Fabry-Perot polymer film ultrasound sensor for high-resolution three-dimensional imaging of biological tissues," *Appl. Opt.* **47**(4), 561–577 (2008).
27. A. Alex, B. Považay, B. Hofer, S. Popov, C. Glittenberg, S. Binder, and W. Drexler, "Multispectral *in vivo* three-dimensional optical coherence tomography of human skin," *J. Biomed. Opt.* **15**(2), 026025 (2010).
28. "Safety of laser products. Equipment classification, requirements and user's guide," BS EN60825–1 (The British Standard Institute, 1994)
29. K. P. Köstli, M. Frenz, H. Bebie, and H. P. Weber, "Temporal backward projection of photoacoustic pressure transients using fourier transform methods," *Phys. Med. Biol.* **46**(7), 1863–1872 (2001).
30. P. A. Khavari, "Modelling cancer in human skin tissue," *Nat. Rev. Cancer* **6**(4), 270–280 (2006).
31. B. E. Treeby, E. Z. Zhang, and B. T. Cox, "Photoacoustic tomography in absorbing acoustic media using time reversal," *Inverse Probl.* **26**(11), 115003 (2010).
32. E. Z. Zhang, J. G. Laufer, P. C. Beard, B. Považay, A. Alex, B. Hofer, and W. Drexler, "Multimodal simultaneous photoacoustic tomography, optical resolution microscopy, and OCT system," *Proc. SPIE* **7564**, 75640U, 75640U-7 (2010).
33. T. Liu, Q. Wei, J. Wang, S. Jiao, and H. F. Zhang, "Combined photoacoustic microscopy and optical coherence tomography can measure metabolic rate of oxygen," *Biomed. Opt. Express* **2**(5), 1359–1365 (2011).

## 1. Introduction

Photoacoustic imaging (PA) is a noninvasive biomedical imaging modality in which laser generated ultrasound waves are used to obtain 3D images of soft tissue [1]. In essence, short (ns) low energy excitation pulses of visible or NIR laser light are delivered to the tissue surface. Absorption of the light by tissue chromophores such as hemoglobin leads to rapid heating followed by an initial pressure increase and the subsequent emission of broadband ultrasonic pulses. By recording the time-of-arrival of the acoustic pulses over the tissue surface, a 3D image of the internally absorbed optically energy distribution—the photoacoustic image—can be recovered. Image contrast is dominated by optical absorption making it well suited for imaging the vasculature due to the strong optical absorption of hemoglobin. As well as imaging vascular anatomy, functional information in the form of blood oxygenation and flow can be obtained: the former by acquiring images at multiple wavelengths and exploiting the spectral differences between oxy and deoxyhemoglobin [2,3], the latter by extracting the acoustic Doppler shift encoded on to photoacoustic waves emitted by moving red blood cells [4–6].

Penetration depth and spatial resolution depend on the mode of operation. In the traditional photoacoustic tomography mode (PAT), full field illumination is employed to excite the photoacoustic waves, which are then detected over the surface using either a single mechanically scanned ultrasound detector or an array of detectors. A 3D image is then reconstructed from the detected signals using an acoustic back propagation algorithm. In this mode, penetration depth, which is limited by optical and acoustic attenuation, can extend to several cm [7]. Spatial resolution is ultimately limited by the frequency dependent acoustic attenuation exhibited by soft tissues and thus scales with penetration depth. For cm penetration depths, sub-mm spatial resolution is possible, decreasing to a few tens of  $\mu\text{m}$  for mm penetration depths. The key advantage of PAT is that, for depths beyond one optical mean free path ( $\sim 1$  mm), it avoids the spatial resolution/depth limitations of purely optical imaging methods that utilize ballistic photons. Several compelling examples of the application of PAT to imaging the structure and function of the vasculature in the mouse brain [8–10], and other organs [11], skin [12] and breast [7] have now been demonstrated. Recently, the so-called “optical-resolution” mode of photoacoustic microscopy (OR-PAM) has been introduced [13]. Unlike the full field illumination used in traditional PAT, OR-PAM employs a focused excitation laser beam to generate the PA waves. A 2D-sequence of acoustic signals or A-lines, each of which represents a depth profile is then used to form a 3D image directly rather than via a reconstruction algorithm. For sub-mm depths in tissue, lateral resolution is defined approximately by the diffraction-limited dimensions of the focused beam and can be of the order of a few microns as in conventional optical microscopy. This enables en face images of individual capillaries [13] and even red blood cells [14] to be obtained with very high lateral resolution. Vertical resolution however, as with traditional PAT, is ultimately limited by frequency dependent acoustic attenuation and thus tends to be lower at around 10  $\mu\text{m}$ . Although exquisite lateral resolution can be achieved, the reliance on ballistic photons means that OR-PAM, unlike PAT, is a strictly superficial imaging technique with a maximum penetration depth of approximately 1 mm.

The dominance of hemoglobin as the primary source of endogenous PA contrast means that PA images typically show the vasculature with high contrast and spatial resolution but relatively little else in the way of the surrounding tissue morphology. Optical coherence tomography (OCT) on the other hand is an imaging modality that obtains its contrast purely optically from reflections at internal surfaces of tissues and thus depends on intrinsic refractive index gradients and therefore extracts signals from all microscopic scatterers independent of their spectroscopic properties [15]. The development of frequency domain OCT (FD-OCT) techniques has led to significant improvements in image acquisition speed and detection sensitivity, compared to the traditional time domain OCT systems. FD-OCT systems measure all the echoes of light returning from various depth points of the sample simultaneously by measuring the depth-dependent modulations of the interference spectrum

[16]. A FD-OCT system can be implemented either using a broadband light source along with a spectrometer as in spectral domain OCT systems or using a narrow bandwidth swept light source along with a photodiode as in swept source OCT systems [17,18].

Both PAT and OCT essentially access depth dependent information by time-of-flight measurements of the respective acoustic or optical wave. However, in contrast to PAT, OCT employs white light interferometry to indirectly record phase modulations in the broadband optical signal via a spectrometer in spectral domain OCT systems, followed by a conversion to the spatial domain by Fourier-transform. The interferometric detection scheme also efficiently suppresses incoherently scattered, non-ballistic light. The transverse resolution of OCT is defined by the numerical aperture of the optics, while the axial resolution is given by the central wavelength and bandwidth and is in the range 1-10  $\mu\text{m}$ . Due to its pure optical approach OCT can be contact-less and permits rapid visualization of densely sampled volumes (typically  $\sim 512^3$  voxels in 1-4 s).

Combining PA imaging and OCT, which are both noninvasive and utilize intrinsic tissue-contrast offers the prospect of exploiting the complementary sources of contrast provided by each modality. Thus, the absorption-based spectroscopic contrast of PA imaging can be exploited to reveal the structure and oxygenation status of the microvasculature to depths of several millimeters whilst the scattering based contrast of OCT can reveal surrounding tissue microstructure. Although OCT can also distinguish blood vessels, it is accomplished by the detection of the motion of red blood cells [19,20], and cannot therefore reveal the presence of static blood found in hemorrhages, vascular occlusions or certain micro vascular pathologies such as tumors where flow stasis can occur. Unlike PA imaging, spectroscopic OCT [21] is not background-free and suffers from sensitivity to speckle, polarization changes and scattering losses that alter the signal components spectrally, which also makes it problematic to quantify blood oxygen using spectroscopic methods.

Although the increased functionality achieved by combining PA imaging and OCT is inherently appealing, the differing detection requirements of PA and OCT signals present a number of instrument design challenges. A previously reported dual mode PA-OCT scanner was configured to operate in OR-PAM mode with the focused PA excitation and OCT probe beams incident on one side of the sample and the ultrasound receiver located on the other [22]. However, this type of transmission arrangement is only suitable for thin samples such as the mouse ear or *ex vivo* specimens that permit access to both sides of the sample. Furthermore, an x-y translation stage was used to mechanically translate the PA and OCT beams thus limiting image acquisition time. An alternative scanning method, also used to image the skin of the mouse ear [23] and subsequently the retina [24], addressed these limitations to some extent. In this approach, co-axial PA excitation and OCT probe beams are optically scanned across the tissue surface using an x-y galvanometer scanner and the PA signals detected on the same side of the sample using a single stationary ultrasound receiver offset from the scan area. As well as providing the more desirable backward mode configuration in which the PA waves are detected on the same side of the tissue that the excitation light is incident, the use of optical scanning provides high acquisition speed with a reported single A-line acquisition time of 0.04 ms [23]. However, the finite angular aperture of the receiver limits the PA field of view (FOV) and only a relatively modest  $3 \times 3 \text{ mm}^2$  scan area has been achieved with this approach. Furthermore, since both of these scanners designs employed the OR-PAM rather than tomographic mode of PA imaging, the photoacoustic penetration depth for non-transparent tissues was limited to less than 1 mm.

In this paper, a new dual mode PA-OCT scanner that has the potential to overcome these limitations is described. Key to its operation is a transparent optically addressed ultrasound sensor based upon a Fabry Perot (FP) polymer film interferometer [25] that is used to detect the PA waves. This sensor has several advantages for combining the two modalities. Firstly, it allows transmission of the OCT probe and PA excitation beams directly through the sensor providing an inherently straightforward backward mode configuration. Secondly, because the PA detection point is scanned across the FP sensor it offers the prospect of avoiding the FOV and SNR limitations of schemes that employ a stationary offset ultrasound receiver [23,24]. It

also means that the PA detection point and OCT probe beam can be co-located so the images produced by each modality are inherently co-registered. Thirdly, the use of 2D optical scanning to spatially map the PA and OCT signals offers the prospect of high-speed acquisition [23]. Finally, compared to previous systems, the scanner provides greater OCT and PA penetration depths—the former due to the longer OCT wavelength used (1050 nm compared to 829 nm [22] or 850 nm [23]) and the latter because the scanner is operated in the tomographic rather than the OR-PAM mode of PA imaging. In this study, depths of up to 5 mm in human and thick mouse skin were obtained with PAT in contrast to the sub-mm depths in the near translucent mouse ear and retina reported by other studies [22–24]. Section 2 describes the design, principles of operation and performance of the scanner. The evaluation of the system by imaging a tissue mimicking phantom to assess image co-registration accuracy, and mouse and human skin to assess its *in vivo* applicability is described in section 3.

## 2. Combined PAT-OCT scanner: principles of operation

A schematic of the dual mode PAT-OCT scanner is shown in Fig. 1. The key elements of the system are a photoacoustic excitation laser system, a Fabry Perot (FP) ultrasound sensor for detecting the PA signals, a 1050 nm spectral domain OCT (SD-OCT) system and a galvanometer based optical scan engine that is used to spatially map the PA and OCT signals.

The photoacoustic excitation laser is a fiber-coupled type I optical parametric oscillator pumped by the 355 nm frequency tripled output of a Q-switched Nd:YAG laser. This provides 8 ns optical pulses over the wavelength range 410–2100 nm at a pulse repetition frequency (PRF) of 50 Hz. The divergent beam emerging from the optical fiber is directed on to the FP sensor head, which is acoustically coupled to the skin surface via a drop of water or gel. The beam diameter incident on the tissue surface was 2 cm. The design and fabrication of the FP sensor has been described previously in detail in [25]. Briefly, it comprises a wedged PMMA substrate with a polymer film Fabry-Perot interferometer (FPI) formed on the lower side—the wedge is required to avoid parasitic interference between the top surface of the substrate and the FPI. The FPI is fabricated by vacuum depositing a thin film structure comprising a 20  $\mu\text{m}$  thick Parylene C polymer film spacer sandwiched between a pair of dichroic soft dielectric mirrors. These mirrors are highly reflective (>95%) between 1500 and 1650 nm but highly transmissive between 590 and 1200 nm. The PA excitation laser pulses in the latter wavelength range can therefore be transmitted through the sensor head and into the underlying tissue. Absorption of the laser energy produces photoacoustic pulses which propagate back to the sensor head where they produce a modulation in the optical thickness of the FPI and hence its reflectivity. The incident photoacoustic wave is then mapped by raster scanning a focused interrogation laser beam at 1550 nm over the surface of the sensor using a galvanometer based x-y scanner. At each point of the scan, the acoustically induced time-varying power modulation of the reflected beam is detected with a fiber coupled InGaAs photodiode-transimpedance amplifier unit connected to a digital storage oscilloscope (DSO, not shown). At the end of the scan the entire set of detected waveforms are downloaded from the DSO to a PC and used to form the image. Since the tomographic mode of PA imaging was used in this study, an acoustic back propagation algorithm [26,27] is required to reconstruct the image from the detected PA signals. Two different algorithms were used variously. The first is a k-space reconstruction algorithm [26], which, although highly computationally efficient, neglects the frequency dependent acoustic attenuation exhibited by soft tissue. The second is based upon a time-reversal method that can compensate for the resolution and SNR degrading effects of acoustic attenuation [27], albeit at greater computational expense. Its benefit is therefore most apparent when imaging more deeply lying anatomical features or tissues exhibiting high attenuation.

The –3dB acoustic bandwidth of the FP sensor is 39 MHz, the FWHM diameter of the sensor interrogation beam is 22  $\mu\text{m}$  and the point-to-point acquisition time 20 ms, limited by the 50 Hz repetition frequency of the excitation laser. For the scan areas (between 1  $\text{cm}^2$  and 2.25  $\text{cm}^2$ ) used in the current study, the lateral instrument line spread function (LSF) lies in

the range 50–100  $\mu\text{m}$  for depths up to 5.5 mm at the center of the scan area [25]. The vertical LSF is, to a first approximation, spatially invariant and dependent largely on the sensor bandwidth. It is estimated to be approximately 20  $\mu\text{m}$ .

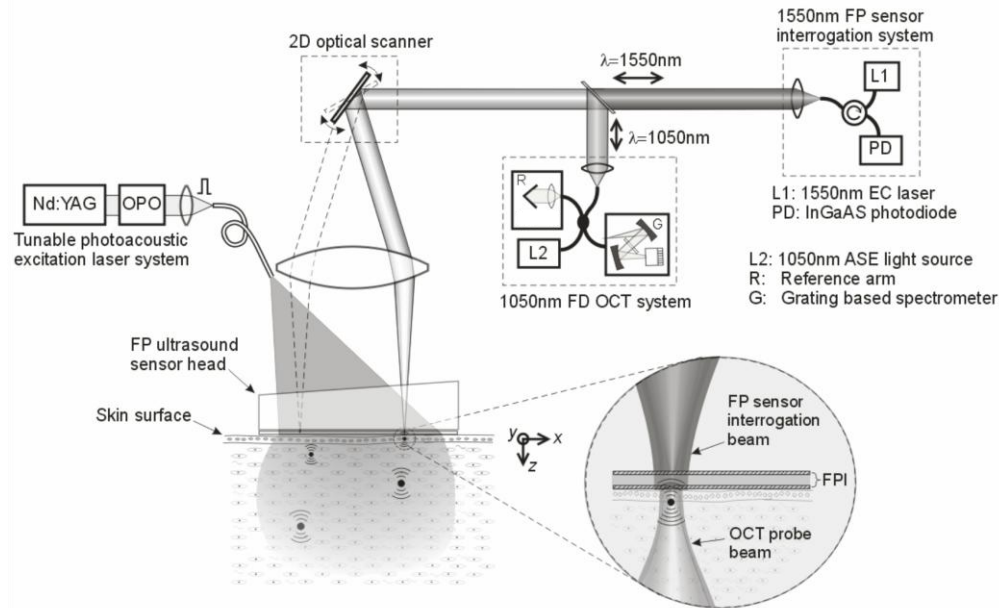


Fig. 1. Multimodal photoacoustic-OCT scanner. The FP sensor head is placed on the surface of the tissue. The output of a tunable OPO laser system provides nanosecond optical pulses which are transmitted through the FP sensor head and into the target. The photoacoustic waves generated by the absorption of the laser energy are detected by the FP sensor which is read out by raster scanning a 1550 nm focused laser beam across its surface. To obtain an OCT image, a probe beam at 1050 nm is combined with the 1550 nm FP sensor interrogation beam so that both are approximately coaxial with each other. Since both beams follow identical paths through scanner and are scanned over the same lateral region, the images produced by each modality are inherently co-registered.

A 1050 nm SD-OCT system was used for OCT image acquisition. 1050 nm has the advantage of greater penetration depth compared to the spectral range 829-870 nm used in previous combined PA-OCT scanners [22,24] due to reduced optical scattering. The system is described in detail in Ref. [26]. Briefly, it comprises a 1050 nm ASE light source (NP Photonics, Tucson, Arizona) with a spectral bandwidth of 70 nm. The source is fiber coupled via a 80:20 beam splitter to the reference arm that incorporates a length adjustable free-space pathway, attenuation filter wheel and dispersion compensator, as well as to the sample arm with the dual axis galvanometric scanner pair and the focusing lens. The return signal is optically processed by a fiber coupled grating based Czerny-Turner spectrometer with the detection being achieved using a 1024 pixel InGaAs line array (Goodrich SUI LDH1, Princeton, New Jersey) with 47 kHz line rate, corresponding to a 14  $\mu\text{s}$  exposure time per OCT-A-line. With 512 A-lines per frame, this camera was capable of recording >90 frames/second. The captured data was then transferred to the frame grabber, PCIe-1427 (National Instruments, Austin, Texas), by the CameraLink connection. The timing of the image acquisition and the scanning of the galvanometric mirrors in the sample arm was controlled using a field programmable gate array, PCI-7830R (National Instruments, Austin, Texas). The raw spectral data was acquired in real-time using an image acquisition program written in LabVIEW (National Instruments, Austin, Texas). This spectral data is then inverse Fourier transformed and further processed to obtain the actual OCT image. The  $\sim 18 \mu\text{m}$  spot size is defined by the numerical aperture of the scanning optics and is equivalent to the lateral

resolution, while the  $<8\ \mu\text{m}$  axial resolution is given by the spectral bandwidth of the system at 1050 nm.

As shown in Fig. 1, a dichroic mirror combines the fiber-coupled 1050 nm output of the ASE source with the 1550 nm FP sensor interrogation beam after their independent collimation so that both beams are approximately co-axial with each other. The two beams are directed via the scanner through a convex lens. Each beam was focused at a slightly different depth by controlling the divergence individually at their respective collimation units: the FP sensor interrogation beam is focused on the plane of the FPI while the OCT probe beam focus is positioned at a slightly greater depth so that it is located just beneath the tissue surface. Although the FPI mirrors are 96% transparent in the 590-1200 nm spectral range, they still reflect a large enough proportion of the 1050 nm OCT probe beam to exceed the dynamic range (covering approximately  $-50$  to  $-120$  dB) of the InGaAs array in the receiving spectrometer (G in Fig. 1). To avoid this, a glass wedge was inserted between the scan lens and the FP sensor head during the OCT scan. This has the effect of tilting the OCT image plane with respect to the plane of the FPI so that the optical reflection from the latter is displaced and rejected by the receiving fiber in the sample arm. It also has the effect of introducing a small fixed lateral offset  $\Delta r$  between the OCT and FP sensor interrogation beam. To estimate  $\Delta r$ , a rectangular grid of known dimensions printed on to an acetate sheet, which provided both scattering and absorption contrast, was imaged by each modality in turn. The lateral displacement of the two images with respect to each other then provides the offset which was used to re-align the PAT and OCT images.

The OCT scan step size ( $12\ \mu\text{m}$ ) was chosen to be smaller than the PAT step size (typically  $>100\ \mu\text{m}$ ) to accommodate the benefit of the higher sampling rate of the OCT system. In addition, the OCT axial increment ( $6\ \mu\text{m}$ ) was smaller than the corresponding PAT increment ( $30\ \mu\text{m}$ )—the latter is given by the product of the sound speed in tissue and the temporal sampling interval of the DSO. Thus, to co-register the images provided by each modality, the reconstructed PAT image data was interpolated to match the more finely sampled OCT data so that the voxel dimensions of both images were identical.

All PAT images were obtained without signal averaging and using an incident fluence below the safe maximum permissible exposure (MPE) for skin [27]. To aid the visualization of deeply lying features, a depth-dependent scaling factor was applied to the reconstructed PAT images to compensate for optical attenuation. Apart from this and the use of an interpolation algorithm, no other image processing was employed. For the OCT images post-processing involved background signal suppression, k-space linearization, dispersion compensation and Fourier-transformation to obtain the spatial signal. To compensate for micro-movements of the samples OCT images were stabilized by registration and frame-wise shifting. To suppress speckle a 3D-low pass filter was applied before the 3D image was rendered. After these post-processing steps, with the prior knowledge of the lateral scanning range and axial depth range, OCT images are rescaled to ensure 1:1 ratio in both axial and lateral directions.

The key advantages of this multimodal system are that it provides a simple and straightforward means of integrating PAT and OCT, a convenient backward mode configuration, the potential speed benefits of optical scanning and inherent co-registration between the two modalities as a consequence of the OCT probe beam and PAT detection beams being co-axially aligned.

### 3. Results

To evaluate the scanner, combined PAT-OCT images of a tissue-mimicking phantom, the skin of a nude mouse and the human palm were obtained.

#### 3.1. Tissue mimicking phantom

A tissue-mimicking phantom was designed to evaluate the system and assess the accuracy of registration between the PAT and OCT images. The phantom comprised 3 layers of turbid gelatin with a number of randomly arranged  $7\ \mu\text{m}$  diameter carbon fibers embedded between

each layer pair. Carbon fibers were chosen because they provide both absorption and scattering contrast and can thus be visualized by both modalities. This permits the degree of image co-registration to be evaluated when the two images are fused together. The gelatin layers contained different concentrations of Intralipid to provide scattering contrast between each layer. The approximate thicknesses  $l$  and reduced scattering coefficients  $\mu_s'$  for each layer were as follows: layer 1;  $l = 0.45$  mm,  $\mu_s' = 2.5$  mm<sup>-1</sup>, layer 2;  $l = 0.53$  mm,  $\mu_s' = 4.6$  mm<sup>-1</sup>; layer 3;  $l = 2.8$  mm,  $\mu_s' = 6.4$  mm<sup>-1</sup>. The OCT and PAT scans were performed consecutively. The OCT scan was performed over an area of  $12 \times 12$  mm<sup>2</sup> in lateral steps of  $12$   $\mu$ m. The OCT depth increment was  $\Delta z = 6$   $\mu$ m. The PAT scan was acquired over the same area but in steps of  $100$   $\mu$ m. The temporal sampling interval was  $20$  ns, which corresponds to a depth increment  $\Delta z$  in the reconstructed PAT image of  $30$   $\mu$ m (assuming a sound speed of  $1500$  m/s). The k-space algorithm was used to reconstruct the images [28]. The photoacoustic excitation wavelength was  $680$  nm, the beam diameter  $2$  cm and the fluence  $6$  mJ/cm<sup>2</sup>. The PAT and OCT data acquisition times were  $7$  minutes and  $\sim 24$  s respectively.

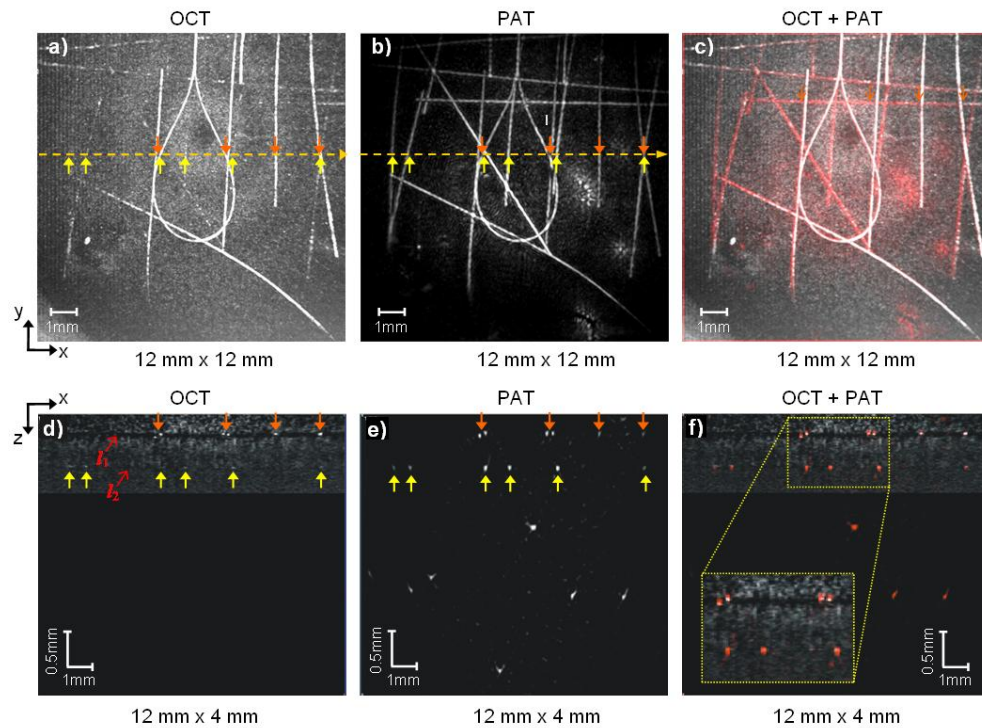


Fig. 2. Images of layered tissue phantom comprising  $7$   $\mu$ m carbon fibers embedded into turbid gelatin (a) OCT x-y MIP image, (b) PAT x-y MIP image (c) Fused OCT-PAT x-y MIP image (d) OCT cross-sectional vertical (x-z) slice along horizontal dotted line shown in (a).  $l_1$  and  $l_2$  indicate the location of the interfaces between layers 1 and 2 and layers 2 and 3 of the phantom respectively (e) PAT cross sectional x-z slice along horizontal dotted line in (b). Orange and yellow vertical arrows in (d) and (e) indicate location of carbon fibers at  $l_1$  and  $l_2$  respectively. (f) Fused OCT-PAT cross sectional x-z slice. Rectangle in lower left hand corner is an expanded view of superficial central region. A fly through movie showing successive x-z slices of the OCT data and fused OCT + PAT image data can be viewed online at ([Media 1](#)).

The distribution of the carbon fibers can be seen in Fig. 2. Figures 2a and 2b show the lateral (x-y) maximum intensity projections (MIPs) of the OCT and PAT 3D image data sets respectively. Figure 2c shows the PAT image (colored in red) overlaying the OCT image. This fused OCT-PAT image illustrates the excellent co-registration between the two images. These MIPs were computed over the depth range  $0 < z < 1.2$  mm so that only the carbon tubes within the maximum OCT penetration depth ( $\sim 1$  mm in this example) are observed in the

PAT image. Figures 2d-f represent single vertical (x-z) cross sectional slices along the horizontal dotted line on the MIPs in Figs. 2a-b for the OCT, PAT and fused OCT-PAT data respectively. A fly-through movie that steps sequentially through all of the x-z slices in the 3D image data set is also available online ([Media 1](#)). Figure 2f and the fly-through movie in particular provide a further demonstration of the excellent registration between the two images. Overall, the registration accuracy is estimated to be less than the dimensions of a single voxel ( $25 \times 25 \times 6 \mu\text{m}^3$ ) over the entire overlap region of  $12 \times 12 \times 1 \text{ mm}^3$  FOV.

### 3.2. Mouse skin

An *in vivo* PAT-OCT image of the skin on the flank of a 5-week-old anaesthetized female hairless mouse was acquired. This was achieved by placing the region of interest on top of the upright sensor head. A drop of water was inserted between the skin and the sensor in order to provide the necessary acoustic and optical coupling. The OCT scan was acquired over an area of  $12.3 \times 13 \text{ mm}^2$  in lateral steps of  $12.5 \mu\text{m}$  at  $\sim 3 \text{ mW}$  of incident power on the sample. Consecutively, the PAT scan was acquired over the same area but in steps of  $100 \mu\text{m}$ . The temporal sampling interval was  $20 \text{ ns}$ , which correspond to a PAT depth increment  $\Delta z$  of  $30 \mu\text{m}$  (assuming a sound speed of  $1,500 \text{ m/s}$ ). As in the phantom experiment described in section 3.1, the k-space algorithm [28] was used to reconstruct the image. The PAT and OCT data acquisition times were 7 minutes and 24 s respectively. The photoacoustic excitation wavelength was  $670 \text{ nm}$ , the beam diameter  $2 \text{ cm}$  and the fluence  $14 \text{ mJ/cm}^2$  and thus below the safe maximum permissible exposure (MPE) of  $20 \text{ mJ/cm}^2$  for skin at this wavelength [27].

Several representations of the reconstructed images are shown in Fig. 3. Figure 3a shows a single vertical slice (x-z) of the fused PAT-OCT image data set. The scattering based contrast of the grey scale OCT image reveals the layered morphology of the skin. This comprises the epidermis that is approximately  $30 \mu\text{m}$  thick, the dermis of thickness  $165 \mu\text{m}$  and the hypodermis, a  $115 \mu\text{m}$  thick layer composed of adipose tissue overlaying skeletal muscle. These dimensions, which were measured from Fig. 3a (at the center of the image) are broadly consistent with those in the literature obtained by histological examination of the mouse skin [29]. Also evident is the panniculus carnosus, a layer of striated muscle that lies between the dermis and hypodermis. The absorption based PAT image (colored red) on the other hand reveals the presence of blood vessels distributed throughout the dermis, hypodermis and subcutaneously. These can be visualized more readily by viewing the fly-through animation available at [Media 2](#). Fig. 3d show lateral (x-y) MIPs of the OCT, PAT and fused OCT-PAT image data respectively over the depth range  $0.24 < z < 0.6 \text{ mm}$ . Within this range lies a star shaped vascular structure located on the dermal - hypodermal border, just above the panniculus carnosus between the dermis and hypodermis. In the OCT MIP image (Fig. 3b), this vascular structure (indicated by the yellow arrows) is barely visible with very weak negative contrast. That it can be seen at all is due to a combination of weak scattering by blood vessels which gives rise to the low negative contrast and the strong attenuation of blood which prevents photons reaching more strongly scattering underlying tissue and otherwise providing positive image contrast. The structure is however clearly visible in the PAT image (Fig. 3c) due to the absorption based contrast of PAT although this in turn means that the surrounding tissue morphology cannot be observed as with OCT.

The fused OCT-PAT image (Fig. 3d) shows both the en-face morphological features of the skin provided by OCT and the blood vessels revealed by PAT with high contrast. Figures 3e-h show volume rendered representations of the fused image data with the OCT image successively resected to reveal the dermal and subcutaneous vasculature in the PAT image. An expanded view of a region of Fig. 3f is depicted in Fig. 3i and perhaps best illustrates the complementary contrast provided by each modality. The layered morphological features of the skin observed in Fig. 3a and part of the star shaped vascular structure containing vessel B1 as well as the deeper lying subcutaneous vascular tree containing vessel B2 are all clearly visible in Fig. 3i. These volume rendered images can also be viewed online in various animated representations at [Media 3](#), [Media 4](#), [Media 5](#). The smallest blood vessel that can be

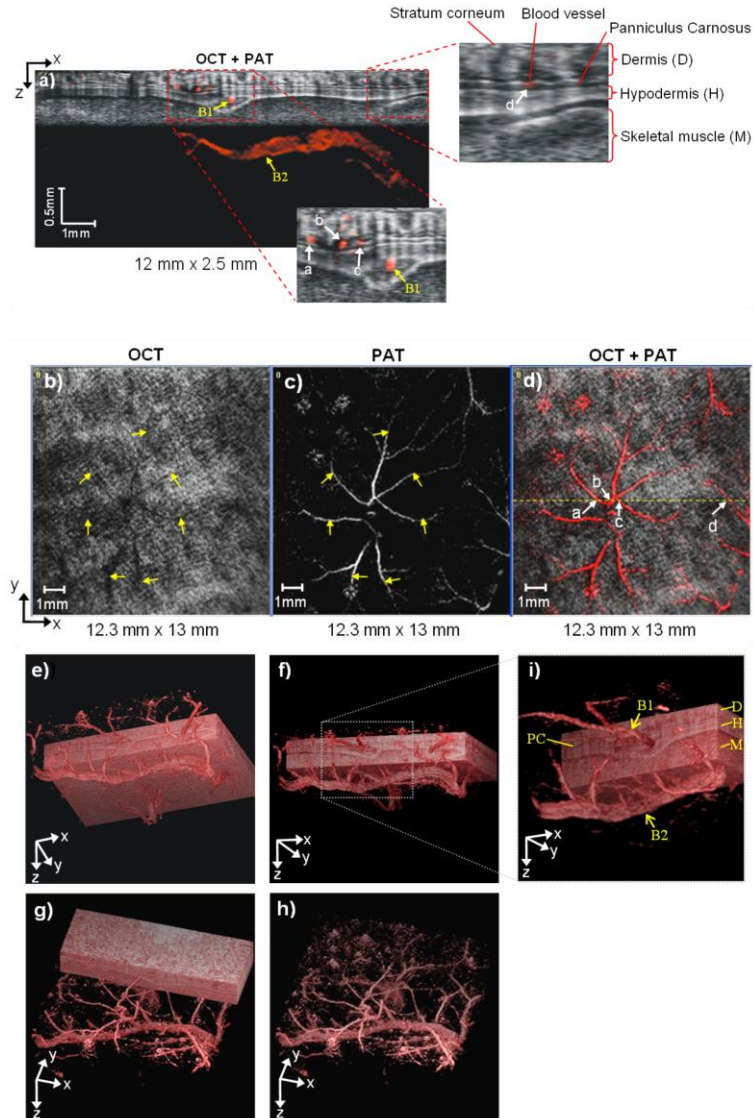


Fig. 3. *In vivo* OCT and PAT images of the mouse skin. (a) Fused OCT-PAT cross sectional vertical ( $x$ - $z$ ) slice. The OCT image (gray scale) shows the layered skin morphology while the PAT image (colored red) shows several superficial blood vessels within the dermis, Panniculus Carnosus, hypodermis (e.g., B1) and the skeletal muscle (B2). The lower inset shows an expanded view of the dermis and hypodermis and a cluster of three blood vessels (a, b and c) which form part of the vascular structure that can be seen in Figs. 3(b-d). The upper inset shows an expanded view of the skin layers and a blood vessel (labeled d) which can also be seen in Fig. 3(d). A fly-through movie that steps through successive  $x$ - $z$  slices over the entire data set can be viewed online at [Media 2](#). (b) OCT ( $x$ - $y$ ) MIP image. The yellow arrows indicate the location of blood vessels forming a star shaped vascular structure. (c) PAT  $x$ - $y$  MIP image. (d) Fused OCT-PAT  $x$ - $y$  MIP image. The horizontal dotted line indicates the location of the  $x$ - $z$  slice depicted in (a). The vessels labeled a-d correspond to those similarly labeled in the two insets in (a). The  $x$ - $y$  MIPs shown in (b-d) were computed over the depth range:  $0.24 < z < 0.6$  mm. (e-h) Volume rendered representations of fused OCT-PAT image data at different viewing angles with the OCT image successively resected. The rendered image volume is  $12 \times 12 \times 2$  mm<sup>3</sup>. (i) Expanded view of (f) over a  $6 \times 6 \times 2$  mm volume showing blood vessels B1 and B2, dermis (D), Panniculus carnosus (PC), hypodermis (H) and skeletal muscle (M) as identified in (a). Animated representations of the volume rendered images can be viewed online at [Media 3](#), [Media 4](#), [Media 5](#).

observed in the various representations of the PAT data in Fig. 3 is 110  $\mu\text{m}$ , the largest approximately 450  $\mu\text{m}$  and the deepest detectable vessel was located 3 mm beneath the surface—the latter can be seen in the x-z fly through movie available online ([Media 2](#)).

### 3.3. Human palm

An *in vivo* image of the subcutaneous vasculature in the palm of a volunteer was obtained. As described in the previous section, the skin was acoustically coupled to the sensor head with a drop of water and successive PAT and OCT scans were undertaken. The photoacoustic excitation wavelength was 672 nm, the beam diameter 2 cm and the fluence 14  $\text{mJ}/\text{cm}^2$  - again below the safe MPE of 20  $\text{mJ}/\text{cm}^2$  for human skin [27]. Consecutively, the PAT scan was acquired over an area of  $14 \times 14 \text{ mm}^2$ , in steps of 120  $\mu\text{m}$ . The temporal sampling interval was 20 ns corresponding to a depth increment  $\Delta z = 30 \mu\text{m}$ . The PAT image was reconstructed using the time-reversal algorithm [30] in order to take advantage of its ability to compensate for acoustic attenuation—necessary in this case due to the greater depth of much of the vasculature compared to that of the mouse skin. The OCT scan was acquired over a  $12.8 \times 12.8 \text{ mm}^2$  area in  $1024 \times 1024$  transverse steps of 12.5  $\mu\text{m}$  and  $\Delta z = 6 \mu\text{m}$  using an incident optical power of  $\sim 3 \text{ mW}$  on the sample. The PAT and OCT data acquisition times were 4.6 minutes and  $\sim 24 \text{ s}$  respectively.

Figure 4a shows a single vertical slice of the fused PAT-OCT image data set in which the stratum corneum, epidermis and dermis can be seen in the gray-scale OCT image. The thicknesses of each of these three layers are  $\sim 300 \mu\text{m}$ , 186  $\mu\text{m}$  and 233  $\mu\text{m}$  respectively measured at the center of the image. The PAT data shows several blood vessels distributed throughout the dermis and the underlying subcutaneous tissue. It also depicts image contrast at the level of the epidermis that is not associated with blood, but absorption by melanin. In this region over most of the FOV it can be seen that the PAT image contrast follows the surface contours of the skin in the OCT image illustrating good image co-registration. On the left hand side of the image, however, a significant vertical offset between the two images is evident. This is most likely to be due to movement of the palm between the two scans. Unlike the mouse skin MIP shown in Fig. 3b, the majority of the blood vessels that are large enough to be clearly differentiated by OCT are beyond its maximum penetration depth - the fine capillaries in the dermal papillae with diameters smaller than 10  $\mu\text{m}$  cannot be clearly identified with either modality. However, beneath the optical artifacts forming vertical arcades in the gray-scale OCT image, portions of vascular structures with negative contrast become visible, while a weak PAT-signal is found there as well. At the dark horizontal stripe in the OCT image underneath the dermal papillae, which appears to be associated with the *rete subpapillare*, there are only a few locations that appear to generate PAT image contrast. This is consistent with the large amount of hemoglobin-free lymphatic vasculature that might be responsible for the dark, tubular structures in the dermis as well.

Figure 4b-d show lateral (x-y) MIPs of the OCT, PAT and fused OCT-PAT image data. The superficial topography of the skin is evident in the OCT image (Fig. 4b) with the fine grooves (*sulci cutis*) on the skin surface that form the dactylogram (fingerprints) clearly apparent. The PAT MIP image in Fig. 4c shows the vasculature, most of which is located at a depth greater than 0.8 mm—the signal originating from the epidermis that is evident in Fig. 3a was removed to reveal the vasculature more clearly. Figures 4e-g show volume rendered representations of the fused OCT-PAT image data at different orientations with the OCT image successively resected. Figures 4f and 4g show the *sulci cutis* on the skin surface as observed in the MIPs as well as the different layers of the skin shown in (a). The smallest blood vessel that can be observed in the various representations of the PAT data in Fig. 4 is 130  $\mu\text{m}$  and the largest approximately 800  $\mu\text{m}$ . The deepest detectable vessel was located 4.8 mm beneath the surface. This vessel cannot be observed directly in Fig. 4c as it is obscured by a more superficial vessel. It is however clearly visible in both the x-z fly through movie and volume rendered animations available online ([Media 6](#), [Media 7](#), [Media 8](#)).

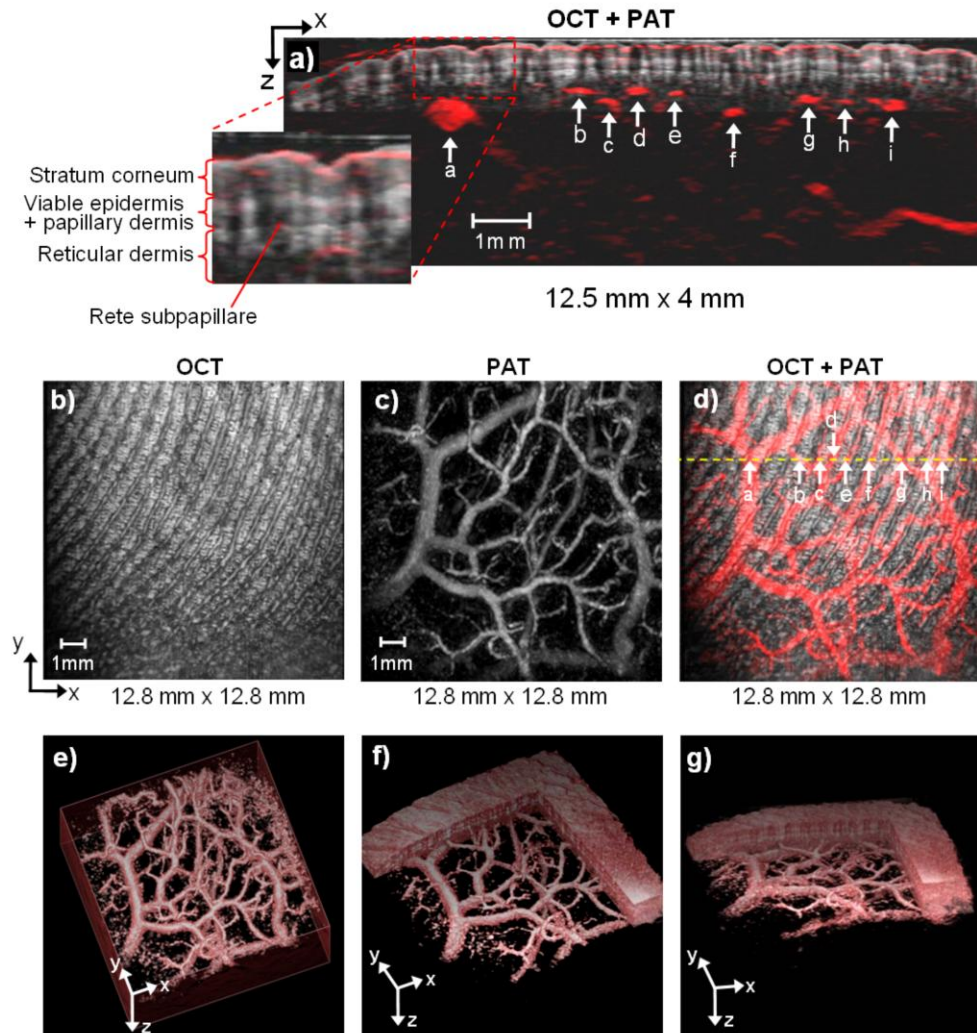


Fig. 4. *In vivo* OCT and PAT images of the human palm. (a) Fused OCT-PAT vertical ( $x$ - $z$ ) slice. A fly-through movie showing successive  $x$ - $z$  slices through the entire data set can be viewed online at [Media 6](#). (b) OCT ( $x$ - $y$ ) MIP image computed over the depth range  $0 < z < 1.2$  mm. (c) PAT  $x$ - $y$  MIP image computed over the depth range  $0 < z < 5$  mm. (d) Fused OCT-PAT  $x$ - $y$  MIP image. Horizontal dotted line indicates the location of the  $x$ - $z$  slice shown in (a) with corresponding locations of blood vessels indicated by the white arrows. (e-g) Volume rendered representations of fused OCT-PAT image data at different viewing angles. The rendered image volume is  $14 \times 14 \times 5$  mm<sup>3</sup>. Animated representations of the volume rendered images can be viewed at [Media 7](#), [Media 8](#).

#### 4. Conclusion

A novel all optical multimodal-imaging scanner that combines PAT with OCT has been demonstrated. It has been shown that the vascular anatomy of the different layers of thick mouse and human skin can be highlighted against the micro-morphology of the skin with axial and lateral resolutions of  $8 \mu\text{m}$  and  $18 \mu\text{m}$  respectively in the OCT image and  $20 \mu\text{m}$  and  $50$ - $100 \mu\text{m}$  in the PAT image. In contrast to previous dual PA-OCT studies which have been limited to imaging highly superficial anatomy ( $<1$  mm deep) in the mouse ear [22,23] or through transparent ocular media to the retina [24], the system described in this paper has

been able to image highly scattering thick mouse and acral human skin to a depth of almost 5 mm.

The key technical advantages of the instrument compared to previous piezoelectric based dual mode OCT-PA systems derive from the transparent optically addressable nature of the FP ultrasound sensor. This provides a convenient and straightforward integration of the two modalities, the desirable backward mode configuration, inherent image co-registration without the use of fiducial markers and the potential speed benefits of 2D optical scanning. The ease of integration is a key factor. Since the OCT probe and FP sensor interrogation beams share the same scan engine, it should be possible to straightforwardly integrate the FP sensor within most existing OCT scanner designs, including high speed parallel approaches. The high degree of inherent image co-registration between the two modalities (to within a single  $25 \times 25 \times 6 \mu\text{m}^3$  voxel), is a consequence of the OCT and PA detection points being, in effect, locked together over the entire scan area. This is particularly relevant to the PA tomography mode of operation (PAT) because in OR-PAM mode, inherent image co-registration can readily be achieved by co-aligning the focused PA excitation beam with the OCT beam. In PAT however, it is the PA detection point, not the excitation beam that needs to be aligned with the OCT beam and it would be difficult to achieve this using a mechanically scanned piezoelectric receiver or array of receivers. The transparent nature of the FP sensor offers a further advantage (irrespective of operating mode) in that the PA detection point is always situated directly above the skin surface irrespective of position within the FOV. The source-detector acoustic propagation path length and thus the acoustic attenuation are minimized and spatially invariant over the FOV. Piezoelectric based dual mode OCT-PA schemes on the other hand generally require some form of acoustic transmission line/beam splitter arrangement to deliver the PA wave to the receiver. This introduces additional signal attenuation and band limiting which are also spatially variant for optically scanned OCT-PA schemes that employ a single stationary offset piezoelectric receiver [23,24]. The latter also offer a somewhat limited FOV ( $<3 \times 3 \text{ mm}^2$ ) due to the directional response of the receiver. By contrast the FOV of the system reported in this paper can be significantly larger, limited only by the maximum angular deflection of the galvanometer and the focal length of the scan lens. Scan areas of  $12.8 \text{ mm} \times 12.7 \text{ mm}^2$  were demonstrated in this study although up to  $40 \times 40 \text{ mm}^2$  is possible with the current scan engine used.

As well as operating in tomography mode, the system can be operated simultaneously in OR-PAM mode as demonstrated in Ref. [31]. Although PAT has the advantage of providing much greater penetration depths than OR-PAM which is limited to sub mm depths, the optical diffraction limited lateral resolution of OR-PAM can be of the order of a few microns and therefore much higher than the acoustically defined lateral resolution of PAT. It is also closer to the lateral resolution provided by OCT and thus advantageous in the sense that with any multimodal system the informational content is greatest when there is parity in the spatial resolutions of the constituent imaging modalities. In the context of skin imaging, combining the two modes therefore offers the prospect of achieving the large penetration depth of PAT to visualize relatively deep large subcutaneous micro vessels whilst OR-PAM could reveal the dermal/epidermal microvasculature at capillary level within the morphological landscape provided by OCT. Combining both modes in this way would be difficult to implement using conventional piezoelectric receivers, not least because of their differing element size and bandwidth requirements and the challenges relating to co-registering the PAT and OCT images referred to above. As well as being able to implement the two PA imaging modes in combination with OCT, the transparent nature of the FP ultrasound sensor provides a convenient platform for integrating other optical imaging modalities such as confocal and multiphoton microscopy. Combining PA imaging with OCT removes the noncontact nature of the latter due to the need to provide acoustic coupling via a liquid or gel. This should not be a significant limitation for most skin imaging applications especially as the acoustic detector does not have to be in direct contact with the skin and can be offset by a layer of water a few mm thick if the skin is highly sensitized for example.

Irrespective of the above technical considerations, a question naturally arises as to the diagnostic benefit and utility of combining PA imaging and OCT. As shown in this study, the complementary contrast of each modality permits both vascular anatomy and tissue micromorphology to be visualized. However, since Doppler OCT and related methods [19,20] can also visualize the vasculature with high spatial resolution (with some exceptions—e.g. if blood flow is negligible), it may be the functional spectroscopic capability of PA imaging that provides the dominant *raison d'être* for combining the two modalities. Spectroscopic PA methods can quantify the concentrations of oxy and deoxyhemoglobin and thus blood oxygen saturation. In addition, when combined with measurements of flow, provided by either by Doppler OCT methods or PA Doppler itself [32], it would also be possible to measure metabolic oxygen rate which is of broad physiological significance in characterizing a variety of pathophysiological processes such as angiogenesis and tissue inflammatory and healing responses. Given these considerations, the system may find application as a tool for high-resolution functional imaging in dermatology. Applications could include studying skin conditions such as tumors, vascular lesions, soft tissue damage such as burns and wounds, inflammatory conditions such as dermatitis and other superficial tissue abnormalities characterized by changes in the skin morphology and the structure and function of the supplying vasculature. It may also find a role in ophthalmology. Here, as suggested in Ref. [33], the well-established ability of OCT to visualize micromorphological features of the retina could be complemented by absorption contrast of PA imaging to quantify retinal blood oxygenation and specific chromophores such as melanin in the RPE.

#### **Acknowledgments**

This research was supported in part by the BBSRC, Cardiff University; DTI grant (OMICRON); AMR grant (AP1110); Medical University Vienna, European Union project FUN OCT (FP7 HEALTH, contract no. 201880), FWF-NFN 'Photoacoustic imaging in biology and Medicine' and CARL ZEISS Meditec Inc., EPSRC and King's College London and UCL Comprehensive Cancer Imaging Centre CR-UK & EPSRC, in association with the MRC and DoH, U.K and the UCL Centre for Advanced Biomedical Imaging. Susanne Binder from the Rudolf Foundation Clinic Vienna, Department of Ophthalmology, Ludwig Boltzmann Institute, Vienna, Austria is acknowledged for support.